Carrier transport properties of nanocrystalline Er3N@C80

doi: info:doi/10.1063/1.4887796

Carrier transport properties of nanocrystalline Er3N@C80

Yong Sun, Yuki Maeda, Hiroki Sezaimaru, Masamichi Sakaino, and Kenta Kirimoto

Citation: Journal of Applied Physics **116**, 034301 (2014); doi: 10.1063/1.4887796
View online: http://dx.doi.org/10.1063/1.4887796
View Table of Contents: http://scitation.aip.org/content/aip/journal/jap/116/3?ver=pdfcov
Published by the AIP Publishing

Carrier transport properties of nanocrystalline $Er_3N@C_{80}$

Yong Sun,[1,a)] Yuki Maeda,[1] Hiroki Sezaimaru,[1] Masamichi Sakaino,[1,b)] and Kenta Kirimoto[2]
[1]*Department of Applied Science for Integrated System Engineering, Kyushu Institute of Technology, Senshuimachi, Tobata, Kitakyushu, Fukuoka 804-8550, Japan*
[2]*Department of Electrical and Electronic Engineering, Kitakyushu National College of Technology, 5-20-1 shii, Kokuraminami, Kitakyushu, Fukuoka 802-0985, Japan*

(Received 14 May 2014; accepted 26 June 2014; published online 15 July 2014)

Electrical transport properties of the nanocrystalline $Er_3N@C_{80}$ with fcc crystal structure were characterized by measuring both temperature-dependent d.c. conductance and a.c. impedance. The results showed that the $Er_3N@C_{80}$ sample has characteristics of *n*-type semiconductor and an electron affinity larger than work function of gold metal. The $Er_3N@C_{80}$/Au interface has an ohmic contact behavior and the contact resistance was very small as compared with bulk resistance of the $Er_3N@C_{80}$ sample. The charge carriers in the sample were thermally excited from various trapped levels and both acoustic phonon and ionic scatterings become a dominant process in different temperature regions, respectively. At temperatures below 250 K, the activation energy of the trapped carrier was estimated to be 35.5 meV, and the ionic scattering was a dominant mechanism. On the other hand, at temperatures above 350 K, the activation energy was reduced to 15.9 meV, and the acoustic phonon scattering was a dominant mechanism. In addition, a polarization effect from the charge carrier was observed at low frequencies below 2.0 MHz, and the relative intrinsic permittivity of the $Er_3N@C_{80}$ nanocrystalline lattice was estimated to be 4.6 at frequency of 5.0 MHz.
 [http://dx.doi.org/10.1063/1.4887796]

I. INTRODUCTION

The endohedral fullerenes have attracted attention for their applications in optics,[1] bio-medicine,[2] electronics,[3] magnetics,[4] and quantum information processing.[5–8] Such applications would require the fabrications of their crystalline structures and metal electrode on the materials. One of their interest properties is a charge transfer from the endohedral atoms to the fullerene cage. The charge transfer has been widely investigated,[9–13] as these materials are expected to display remarkable electronic and structural properties associated with this charge transfer. Among these endohedral fullerenes, trimetallic nitride endohedral fullerenes (TNEFs), such as $Sc_3N@C_{80}$ and $Er_3N@C_{80}$, can be obtained in large yield and evaporated onto heated substrates[14] because of their thermal stabilities.[15,16] After the extensive studies in theoretical calculations and experimental analysis for isolated molecule of the materials, few fundamental investigations are now carried out on electrical properties of the endohedral fullerenes in condensation states, recently.

The self-assembled island formations of $Sc_3N@C_{80}$ and $Er_3N@C_{80}$ molecules on Au(111) and Ag/Si(111) surfaces have been investigated.[17] Charge transport properties of the $Sc_3N@C_{80}$ film prepared by drop-casting its CS_2 solution on the quartz substrate, such as carrier mobility and energy band structure, have also been studied.[9] The $Sc_3N@C_{80}$ thin film exhibits a low electron mobility of $5.7 \times 10^{-3}\ cm^2\ V^{-1}\ s^{-1}$ under normal temperature and atmospheric pressure. However, it is not easy so far as to obtain enough amounts of the endohedral fullerenes to measure physical and electrical characters. Therefore, the difficulties in fabricating crystals and actual devices still remain, and a discussion of the carrier transport properties through the TNEFs/metal contact was not carried out in detail.

In this study, we prepared a nanocrystalline $Er_3N@C_{80}$ solid sample by pressing powder material to a pellet with two gold electrodes. The temperature-dependent conductivity of the $Er_3N@C_{80}$ sample was measured in the condition of various applied electric fields. In addition, the resistance and capacitance of the Au/$Er_3N@C_{80}$/Au structure were obtained at various d.c. bias and a.c. voltages. The results obtained in this study indicate that the charge transfer leads to a high conductivity of the nanocrystalline $Er_3N@C_{80}$ solid as well as a low contact resistance with gold electrodes. The energy levels at the $Er_3N@C_{80}$/Au interface and the transport properties of the charge carriers passing through the sample will be discussed.

II. EXPERIMENTAL

$Er_3N@C_{80}$ powder with purity > 95 wt. % was purchased from LUNA Innovations to make a sample specimen for measurement.[18,19] The $Er_3N@C_{80}$ powder was pressed into a pellet at room temperature at 1.25 GPa for 50 min. The so formed pellet was 5.0 mm in diameter and 0.55 mm in thickness. Two gold electrodes on the surfaces of the sample were prepared using an Au nano-particle paste (NAU-K05B, Daiken), and the sample was annealed at temperature of 500 K in vacuum for 30 min. Prior to electrical measurements the powder and pellet samples were characterized by

a)E-mail address: sun@ele.kyutech.ac.jp
b)Present address: Department of Vehicle Production Engineering, NISSAN MOTOR CO. LTD., 560-2, Okatsukoku, Atsugi-city, Kanagawa-pref. 243-0192, Japan.

an x-ray photoemission spectroscopy (XPS; AXIS-NOVA, SHIMATSU/KRATOS) and x-ray diffraction (XRD; JEOL JDX-3500 K). In the XPS analysis, the beam diameter of Al Kα line was 55 μm, and the binding energy resolution was 0.15 eV.

In the electrical measurements, the current passing through the sample was measured using a digital electrometer (ADVANTEST R8252) with a current resolution of 1.0 fA at various d.c. bias voltages from 0.001 to 3.0 V. The pellet sample was set in a vacuum chamber of a cryostat during the electrical measurements. The base pressure of the vacuum chamber was less than 10^{-5} Pa. The current measurements were carried out in the course of heating up or cooling down process between the temperatures from 100 K to 500 K. The rate of heating or cooling was 0.14 K min^{-1} with a stepwise increment of 1.0 K.

The impedance of the sample was measured at room temperature in atmosphere to separate the bulk and interface resistances in the sample by using a Cole-Cole plot method. The impedance $Z = Z' + jZ''$ was used to characterize both resistance and capacitance by plotting the imaginary part $-Z'' = -\mathrm{Im}[Z]$ versus the real part $Z' = \mathrm{Re}[Z]$ of the impedance. The important information pertinent to the $Er_3N@C_{80}$/Au structure can be obtained.

III. RESULTS

Three x-ray photoemission spectra of the pellet sample at room temperature were show in Fig. 1. They were obtained from the surface of the $Er_3N@C_{80}$ sample before and after Ar^+ ion sputtering for 10 and 30 s, respectively. Eight peaks at binding energies of 9, 56, 98, 167, 242, 285, 531, and 999 eV were observed in the spectra. The 9 eV peak is attributed to a photoemission from 4*f* electrons of Er atoms. The double peaks at 56 and 98 eV are the photoemissions from Er MVV, and the 167 eV peak is from Er 4*d*. The peak around 285 and 531 eV comes from C 1*s* and O 1*s* core level, respectively. The peaks around 999 eV correspond to O KLL Auger emission. Also, the peaks around 240 eV observed after the Ar^+ ion sputtering are from Ar $2p^{1/2}$ and $2p^{3/2}$ core levers. In the XPS spectra, the Ar^+ ion sputtering causes both the decrease in the O-related peaks and the increases in Er and C-related peaks. Namely, the oxygen atoms adsorb only on the surface of the pellet sample. From the spectrum after the 30 s Ar^+ ion sputtering, atomic ratio of Er/C is evaluated to be 3.64 at. %, close to the stoichiometric ratio of 3.61 at. % for $Er_3N@C_{80}$. Also, the photoemission from the N atoms cannot be detected due to its smaller relative sensitivity factor (RSF, 0.505) and concentration as well as encapsulation in the C_{80} cage. Although the RSF of C 1*s* is also small, 0.318, its XPS intensity is somewhat strong because of the abundant concentration of C atoms in the $Er_3N@C_{80}$ molecules.

The enlarged photoemission spectra from O 1*s* core level were shown in Fig. 2 for various Ar^+ ion sputtering times. The Ar^+ ion sputtering results in the decrease of the peak intensity and the shift of the peak toward the low energy side. The results indicate that the oxygen atoms adsorbed only on the surface of the pellet sample as well as there is an electronic interaction between the adsorbed oxygen atoms.

The photoemission spectra from the Er 4*d* core level were enlarged in the energy scaling and they were plotted in Fig. 3. The peak at binding energy of 169.5 eV does not change with increasing sputtering time. This result suggests a weak electronic interaction between the Er atoms with adsorption oxygen atoms on the surface of the C_{80} cage. On the other hand, the peak intensity increases after the Ar^+ ion sputtering due to desorption of the adsorbed oxygen atoms. Figure 4 shows the photoemission spectra from the C 1*s* core level in the enlarged binding energy scale. The intensity of the C 1*s* peak increased after the Ar^+ ion sputtering but no significant peak shift was observed. This may be related to the conjugation effect of π electrons on the surface of the C_{80} cage.

XRD patterns of the as-received $Er_3N@C_{80}$ powder sample were shown in Fig. 5. Several diffraction peaks can

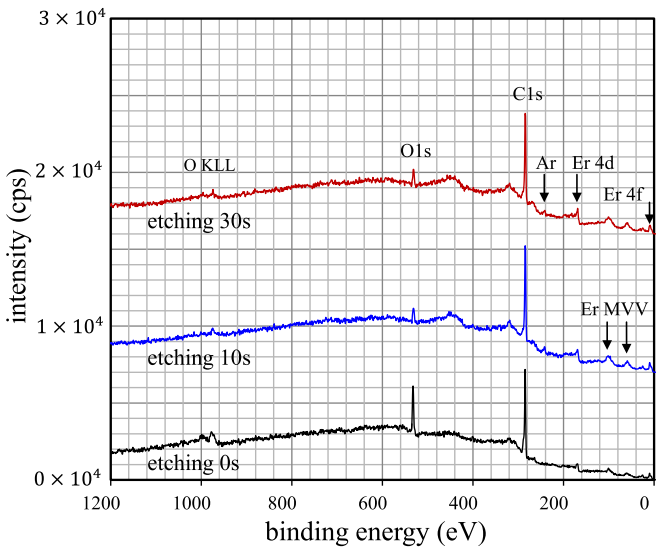

FIG. 1. X-ray photoemission spectra of the nanocrystalline $Er_3N@C_{80}$ sample prepared at a pressure of 1.25 GPa. The spectra are detected on the surface of the sample before and after Ar^+ ion sputtering for 10 and 30 s.

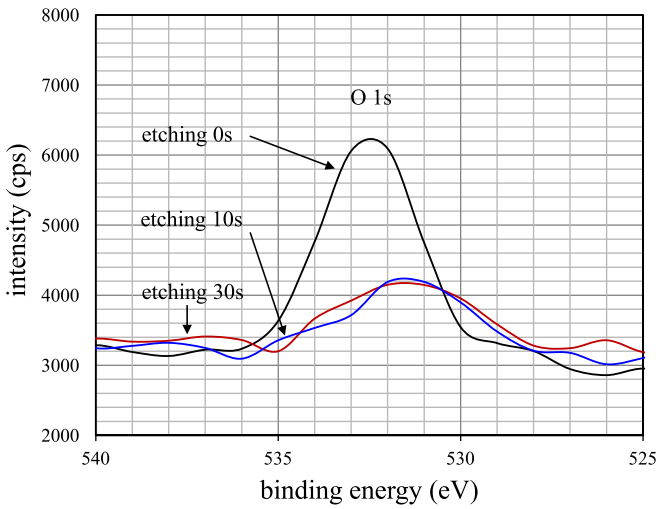

FIG. 2. Enlarged x-ray photoemission spectra from O 1*s* core level before and after Ar^+ ion sputtering for 10 and 30 s.

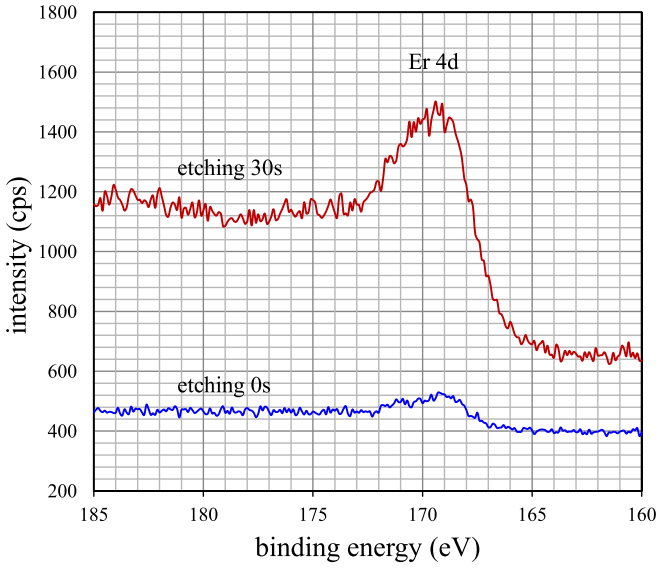

FIG. 3. Enlarged x-ray photoemission spectra from Er 4*d* core level before and after Ar^+ ion sputtering for 30 s.

be recognized for the pattern, a strong peak at $2\theta = 9.30$ deg and four broad peaks centered at $2\theta = 18.00$, 25.70, 32.95, and 50.80 deg. The enlarged XRD pattern of the $2\theta = 9.30$ deg peaks was shown in the inset to Fig. 5. As seen in the inset figure, no significant asymmetry is observed for this diffraction peak. The $2\theta = 9.30$ deg peak was ascribed to the diffraction from (111) planes of a face-centered cubic (fcc) crystal structure with a lattice constant of 1.65 nm. The grain size of the as-received powder sample was estimated to be 4 nm from the full width at half-maximum (FWHM) of the (111) peaks.

Cole − Cole plots of the a.c. impedance of the Au/$Er_3N@C_{80}$/Au structure at room temperature at the peak voltage of 1.0 V at the d.c. bias voltage of 0.0 V was shown in Fig. 6. The Cole − Cole plot exhibits a semicircle, indicating that the impedance is reflected only by both resistance and capacitance of the bulk $Er_3N@C_{80}$ sample and its interfacial component can be ignored. The bulk resistance and

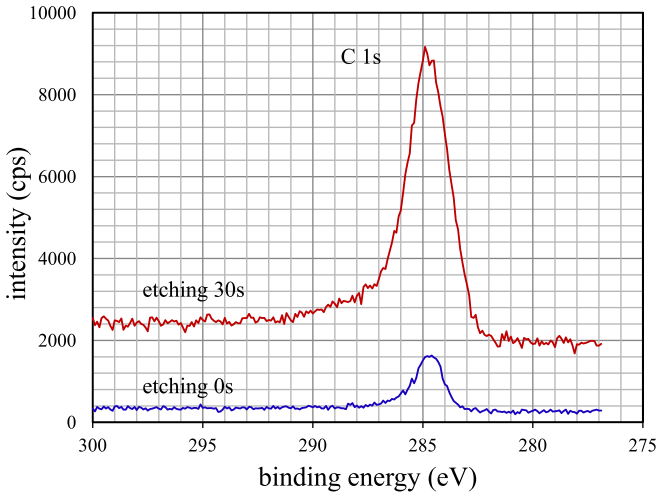

FIG. 4. Enlarged x-ray photoemission spectra from C 1*s* core level before and after Ar^+ ion sputtering for 30 s.

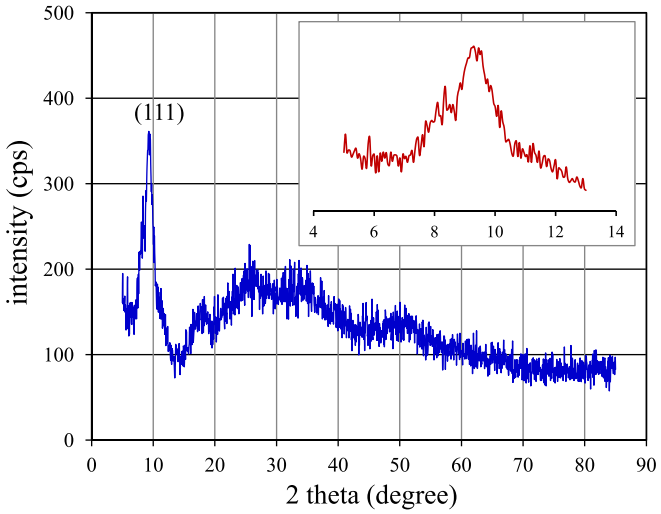

FIG. 5. X-ray diffraction patterns of the as-received $Er_3N@C_{80}$ powder. The inset shows the enlarged patterns of the (111) diffraction peaks.

capacitance are defined from the real and image parts of the impedance, their values are $7.28 \times 10^5\ \Omega$ and 1.08×10^{-12} F at the frequency of 300 KHz. We must also point out that the bulk resistance of the sample in atmosphere increases due to the adsorption of gas molecules, which results in the localization of the charge carrier.

The current-voltage (*I-V*) characteristics of the Au/$Er_3N@C_{80}$/Au sample at temperatures of 300 and 500 K were shown in Fig. 7. The currents passing through the sample at 300 and 500 K can be fitted as a quadratic function of the d.c. bias voltage in the range of 0.001–3.0 V. The quadratic *I-V* characteristic is related to a hopping conductance of the charge carrier in molecular materials[20] and is distinctly different to an exponential *I-V* characteristic of the Schottky barrier. The results in Figs. 6 and 7 indicate that the contact between the nanocrystalline $Er_3N@C_{80}$ sample and the Au electrode is ohmic and the electron affinity of the $Er_3N@C_{80}$ sample is larger than the work function of gold metal. Therefore, we can characterize directly the carrier transport properties of the sample by measuring its field and temperature-dependent *I-V* characteristics. In general, when

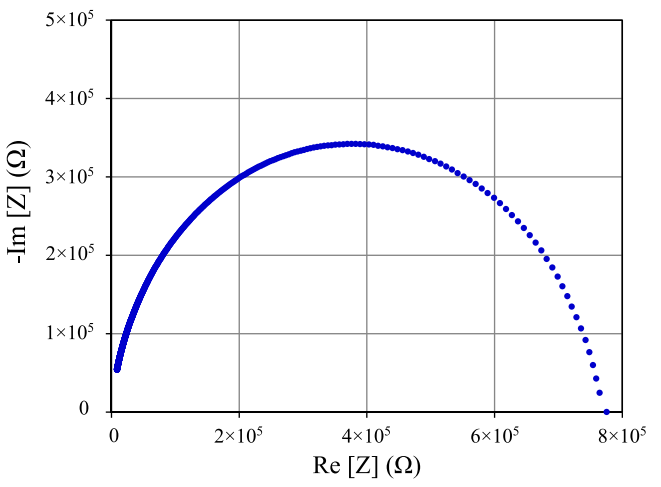

FIG. 6. Cole-Cole plot of the impedance of the Au/$Er_3N@C_{80}$/Au structure at room temperature at a.c. voltage of 1.0 V at d.c. bias voltage of 0.0 V.

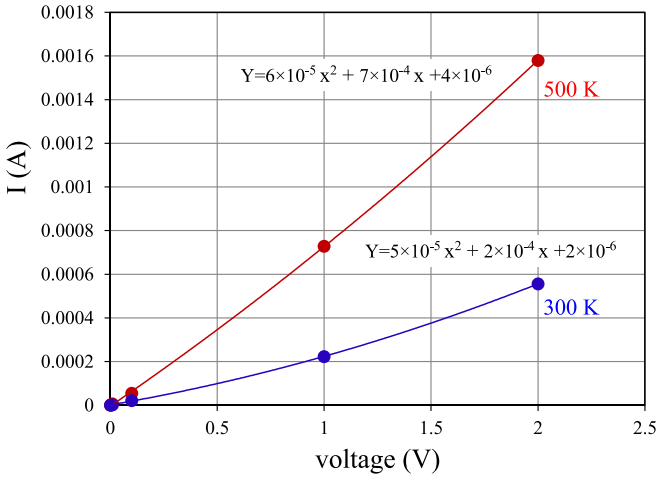

FIG. 7. Current-voltage characteristics of the Au/$Er_3N@C_{80}$/Au structure at 300 and 500 K.

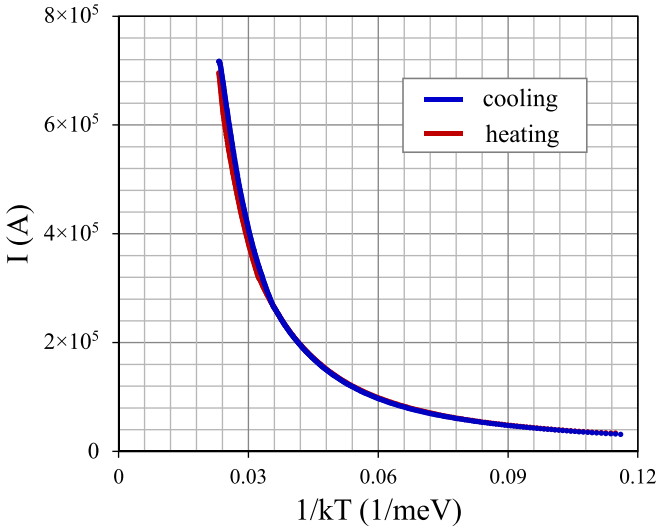

FIG. 8. The current passing through the Au/$Er_3N@C_{80}$/Au structure as a function of temperature during heating up and cooling down process.

the electrical transport is governed by space charge limited conduction (SCLC) mechanism,[21,22] the current I is represented by

$$I(E, T) = \frac{9S\varepsilon_r\varepsilon_0\mu(E, T)E^2}{8L}, \quad (1)$$

where E is the strength of the applied electric field, T is the absolute temperature, S is the area of the electrode, L is the thickness of the sample, $\varepsilon_r\varepsilon_0$ is the permittivity, and $\mu(E, T)$ is the mobility of the charge carrier in the sample. Namely, the current I is a quadratic function of the electric field $E = V/L$. Here, the mobility $\mu(E, T)$ is field and temperature dependent and is described as follows:[23]

$$\mu(E, T) = \left[\frac{qR^2\nu}{kT}\right] \exp\left\{-\frac{\epsilon_a - \Delta\epsilon_a}{kT}\right\}, \quad (2)$$

where R is the mean free pass of the charge carrier, ν is the thermal vibration frequency of the host molecule, q is the unit of electronic charge, ϵ_a is the activation energy of the trapped charge carrier, and $\Delta\epsilon_a = (E/4\pi\varepsilon_r\varepsilon_0 q)^{1/2}$ the change of ϵ_a after the electric field E is applied. Here, $\varepsilon_r\varepsilon_0 = \varepsilon_\infty\varepsilon_0$ is the permittivity at high frequency. One can notice from Eq. (2) that the ν is dependent of temperature. Therefore, Eq. (2) can be written as follows:

$$\mu(E, T) = T^\alpha \exp\left\{-\frac{\epsilon_a - \Delta\epsilon_a}{kT}\right\}, \quad (3)$$

where α is a constant depending on scattering mechanism of the charge carrier during the electrical transport process.

The current I at various d.c. bias voltages were measured as a function of temperature during heating up and cooling down processes. Arrhenius plots of $I \sim 1/kT$ at the d.c. bias voltage of 1.0 V were plotted in Fig. 8. The current I increases with temperature in the range of 100–500 K and cannot been fitted using single exponential function. The result indicates that there is different α and ϵ_a at high and low temperature sides. We have conformed from the Arrhenius plots of $I \sim 1/kT$ that the current I can be fitted by using $\alpha = -1.5$ for high temperature side and $\alpha = 1.5$ for low temperature side, respectively.

Arrhenius plots of the $I \times T^{1.5} \sim 1/kT$ for high temperature side and $I \times T^{-1.5} \sim 1/kT$ for low temperature side at the d.c. bias voltage of 1.0 V during heating up and cooling down processes were shown in Figs. 9(a) and 9(b). The good linear relationships in the Arrhenius plots indicate that the electrical transport properties of the nanocrystalline $Er_3N@C_{80}$ sample can be explained using Poole-Frenkel model.[23] The $\alpha = -1.5$ at high temperature side and $\alpha = 1.5$ at low temperature side suggest various scattering mechanisms of the charge carrier in the sample. On the basis of the Arrhenius plots at various d.c. voltages, we obtained the activation energies of the trapped charge carrier to be $\epsilon_a = 15.9$ meV for high temperature side and $\epsilon_a = 35.5$ meV for low temperature side. The $\Delta\epsilon_a$ is in the range of $1.6 \times 10^{-2} \sim 8.8 \times 10^{-1}$ meV and can be ignored as compared with ϵ_a.

The dielectric properties of the nanocrystalline $Er_3N@C_{80}$ sample were characterized by measuring its impedance spectra. In general, an equivalent electric circuit of a metal/semiconductor/metal system can be represented by a parallel combination of the interfacial resistance (R_i) and capacitance (C_i) in series with a parallel arrangement of the bulk resistance (R_B) and capacitance (C_B).[24–26] In this study, both R_i and C_i are small enough and can be ignored. The bulk resistances at frequencies of 6.25 KHz and 5.0 MHz were plotted in Fig. 10(a) as a function of the d.c. bias voltage. R_B is constant at frequency of 5.0 MHz but it decreases with increasing d.c. bias voltage at frequency of 6.25 KHz. On the other hand, the bulk capacitances at frequencies of 6.25 KHz and 5.0 MHz were plotted in Fig. 10(b) as a function of the d.c. bias voltage. C_B is also constant at 5.0 MHz but it decreases with increasing d.c. bias voltage at frequency of 6.25 KHz. The dielectric properties as shown in Fig. 10 indicate that there are two kinds of polarization mechanisms in the nanocrystalline $Er_3N@C_{80}$ sample. One is related to the conducting charge carriers, which contribute to the

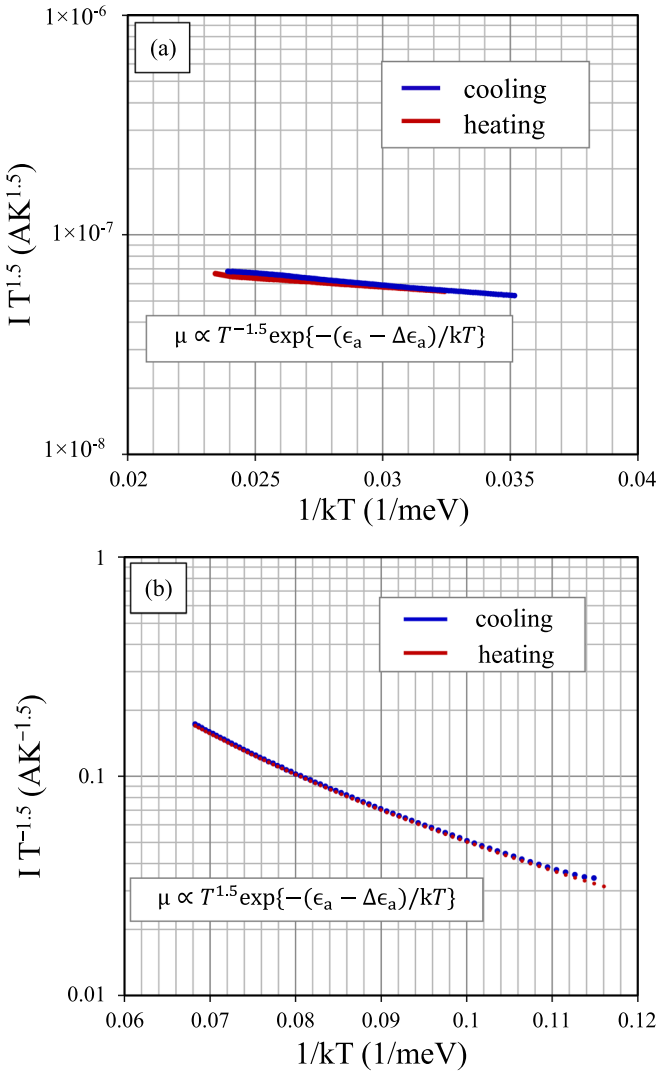

FIG. 9. (a) Arrhenius plots of $I \times T^{1.5} \sim 1/kT$ at high temperature side during heating up and cooling down process. (b) Arrhenius plots of $I \times T^{-1.5} \sim 1/kT$ at low temperature side during heating up and cooling down process.

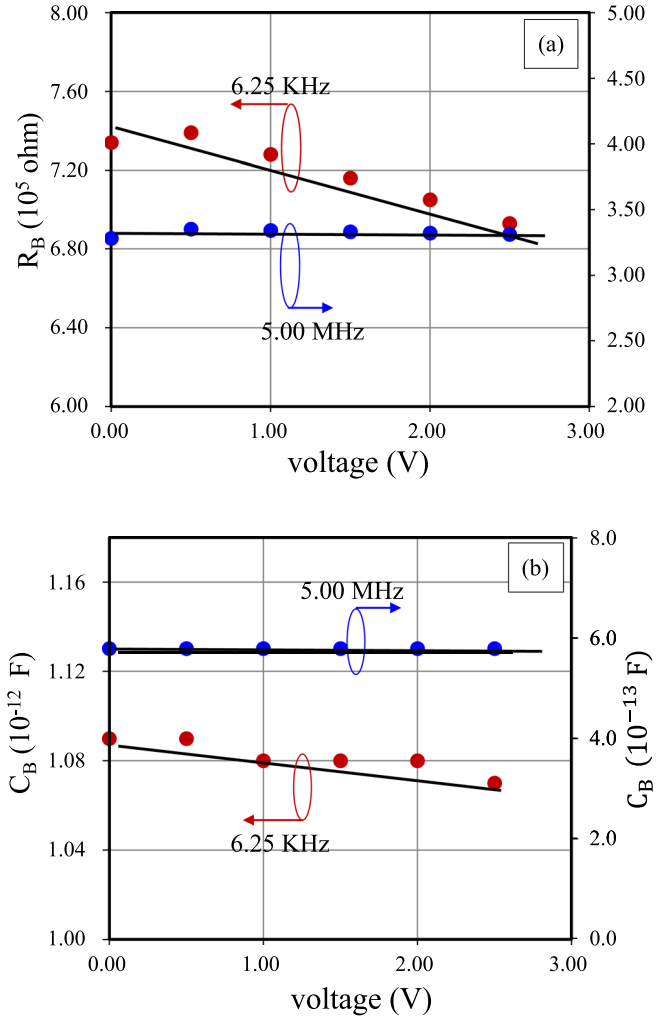

FIG. 10. (a) Bulk resistances of the nanocrystalline $Er_3N@C_{80}$ sample at 6.25 kHz and 5 MHz as a function of d.c. bias voltage. (b) Bulk capacitances of the nanocrystalline $Er_3N@C_{80}$ sample at 6.25 kHz and 5 MHz as a function of d.c. bias voltage.

sample polarization at lower frequencies only because of a low mobility of the carrier in the sample. Other one is related to the dielectric properties of the $Er_3N@C_{80}$ crystal lattice, which contributes to the sample polarization in the higher frequencies.

The bulk resistance R_B and capacitance C_B were defined as these of the resistance and capacitance at maximum of the Cole-Cole curve. The time of the charge carrier passing through the sample, the resonance time τ, can be obtained from a relationship of $\omega\tau = 1$, where $\omega = 2\pi f$ and $\tau = R_B C_B$, and f the frequency of the carrier passing through the sample.

The relative permittivities of the nanocrystalline $Er_3N@C_{80}$ sample at various a.c. voltages at the d.c. bias voltage of 0.0 V were plotted in Fig. 11 as a function of the a.c. frequency. The permittivity decreases rapidly with increasing a.c. frequency from 8.5 at 6.25 KHz to 4.6 at 5.0 MHz. It becomes constant at higher frequencies. No significant difference due to the a.c. bias voltage is observed. The larger permittivities at low frequency side are related to the polarization from the charge carrier. On the other hand,

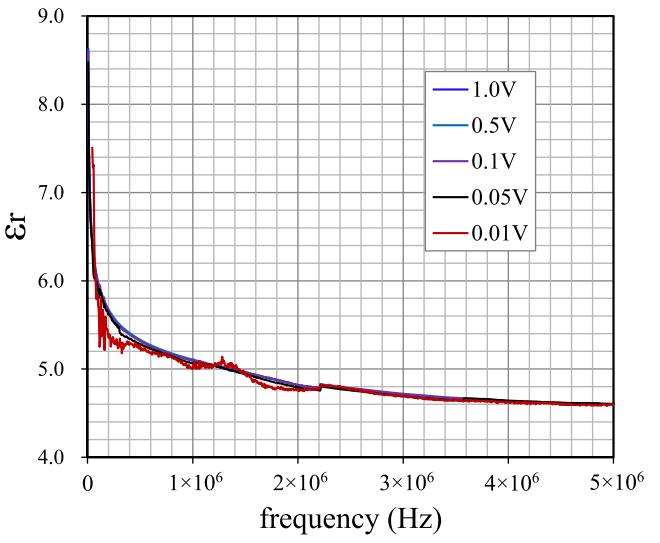

FIG. 11. Relative permittivities of the nanocrystalline $Er_3N@C_{80}$ sample at various d.c. bias voltages as a function of frequency.

the smaller permittivities at high frequencies are due to the polarization of the $Er_3N@C_{80}$ crystal lattice only.

IV. DISCUSSION

A. Energy band structure of the $Er_3N@C_{80}$/Au interface

From the results in Figs. 6 and 7, we can conclude that the $Er_3N@C_{80}$/Au interface corresponds to an Ohmic contact, namely, there is not the Schottky barrier for the carrier transport passing through the interface. The $Er_3N@C_{80}$ sample is *n*-type semiconductor with the electron affinity larger than the work function of gold metal, 5.1 eV.[27] Tang *et al.* have calculated the energy levels of the C_{80} and $Er_3N@C_{80}$ molecules with I_h symmetry by using density function theory (DFT).[28] The highest occupied molecular orbital-lowest unoccupied molecular orbital (HOMO-LUMO) gap and the LUMO level are 0.05 eV and −3.80 eV for C_{80} and 0.13 eV and −5.40 eV for $Er_3N@C_{80}$ molecule, respectively. In their theoretical results, the electron affinity of the $Er_3N@C_{80}$ molecule is larger than the work function of gold metal. This is consistent with our experimental results in this study because no Schottky barrier was observed at the $Er_3N@C_{80}$/Au interface. Namely, the ohmic contact at the $Er_3N@C_{80}$/Au interface indicates a large electron affinity of the nanocrystalline $Er_3N@C_{80}$ solid.

As far as we know, there are still no experimental results on the energy structure of the $Er_3N@C_{80}$ crystal. At present, the surface potential analysis is an effective method to investigate the electronic structures of fullerene-related materials.[29–31] Several experimental results indicated that the shift of the surface potential, the difference between the work function of metal and the electron affinity of fullerene-related materials, depends on film thickness of the materials.[29,32–34] Therefore, the energy band structure of the $Er_3N@C_{80}$ material may depend on its crystallographic and interfacial properties.

B. Dielectric properties

As shown in Fig. 11, the relative permittivity of the nanocrystalline $Er_3N@C_{80}$ sample decreases from 8.5 at 6.25 KHz to 4.6 at 5.0 MHz. At low frequencies, the resistance and capacitance of the $Er_3N@C_{80}$ sample decrease with increasing d.c. bias voltage as shown in Fig. 10. The results indicate that polarization properties of the nanocrystalline $Er_3N@C_{80}$ sample at low frequencies are related to its electrical properties such as the mobility and concentration of the charge carrier. For example, the time τ is 1.44×10^{-6} s at 6.25 KHz and 1.94×10^{-7} s at 5.0 MHz, respectively. The period of the a.c. voltage, t, is 1.6×10^{-4} s for 6.25 kHz and 2.0×10^{-7} s for 5.0 MHz, respectively. It is clear that $\tau\,(1.44 \times 10^{-6}\,\mathrm{s}) \ll t(1.6 \times 10^{-4}\,\mathrm{s})$ at 6.25 KHz and $\tau\,(1.94 \times 10^{-7}\,\mathrm{s}) \cong t\,(2.0 \times 10^{-7}\,\mathrm{s})$ at 5.0 MHz. This fact indicates that the polarization of the charge carrier affects the dielectric properties of the sample at lower frequencies only.

At present, the permittivity of the $Er_3N@C_{80}$ solid has not been reported as far as we know. It is well known that the crystal C_{60} lattice has an intrinsic permittivity of 4.4.[35,36] The dipole dynamics in the endohedral metallofullerene $La@C_{82}$ have been studied theoretically and experimentally.[37,38] In the solid state, pure $La@C_{82}$ has a fcc structure at room temperatures. The C_{82} cage with C_{2v} symmetry is highly disordered in high-symmetry lattice. In the $La@C_{82}$ molecule three electrons transferred to the C_{82} cage from the endohedral La atom. Electrostatic interactions result in the endohedral La^{3+} ion being located close to the cage edge and an important consequence of such an arrangement is a molecular electric dipole. At room temperature, the relative permittivity of the $La@C_{82}$ molecular solid is 40 at 100 Hz and 25 at 1.0 MHz. The large permittivity is due to a dynamic response of the $[La]^{3+}[C_{82}]^{3-}$ dipole in the $La@C_{80}$ molecule. In this study, the intrinsic permittivity of the $Er_3N@C_{80}$ sample, 4.6, is larger than that of C_{60} crystal, 4.4. This may be related to the electron transfer from Er_3N cluster to C_{80} cage because of the formation of three dipoles, $[ErN]^{3+}[C_{80}]^{3-}$, between the cluster and the C_{80} cage. On the other hand, the permittivity of the $Er_3N@C_{80}$ is smaller than that of $La@C_{80}$ because of a high asymmetry of $[Er]^{+}[N]^{-}$ and $[ErN]^{3+}[C_{80}]^{3-}$ as compared with $[La]^{3+}[C_{82}]^{3-}$.

In addition, the dielectric properties of the fullerene-related materials are strongly affected by the adsorptions of O and N atoms.[39,40] The fact that both C_{60} and oxygen molecules are non-polar, together with the evidence of reversible oxygen diffusion into the C_{60} solid, strongly suggest that these dipoles arise from charge transfer between oxygen molecules and C_{60} cages. The amount of this charge transfer is bound to be very small, reflecting the fact that the electron affinities of both C_{60} and molecular oxygen are relatively high. Due to the large size of the C_{60} molecules, this small charge transfer creates large dipole moments. Since the electron affinity of the C_{60} molecule, 2.65 eV,[41] is considerably higher than that of molecular oxygen, 0.45 eV,[42] one might expect oxygen to be the donor and C_{60} the acceptor of electrons.

C. Electrical transport properties

Based on the measurement results of temperature-dependent current as shown in Figs. 7–9, we can include that the conductivity of the $Er_3N@C_{80}$ sample is governed by both mobility and concentration of the charge carrier. There are different temperature dependences on the mobility and concentration of the carrier at high and low temperature sides. At high temperature side, the activation energy of the trapped carrier is 15.9 meV as well as the temperature dependence of the mobility is $\mu \propto T^{-1.5}$. This temperature dependence suggests an acoustic phonon scattering mechanism[43] during the carrier transport. On the other hand, at low temperature side, the activation energy is 35.5 meV as well as the temperature dependence of the mobility is $\mu \propto T^{1.5}$. The activation energy of the trapped carrier becomes large and there is a dominant ionic scattering process[44] at low temperature side.

It is well known that a phase transition between single cubic (sc) and fcc phases in the C_{60} crystal occurs when temperature varies passing through 260 K.[45,46] This transition is described to be due to a free rotation of C_{60} molecules on its crystal lattice. Because of the same molecular symmetry, I_h,

between the C_{60} and C_{80} cages, a similar phase transition may occur in the $Er_3N@C_{80}$ crystal phase. This transition temperature may be above 350 K due to a large mass and diameter of the $Er_3N@C_{80}$ molecule.

It has also been reported that the energy band structure of the C_{60} crystal changes when the sc-fcc phase transition occurs.[47] Similar changes on the energy band structure may occur in the $Er_3N@C_{80}$ crystal phase. This change results in the decrease of the activation energy of the trapped carrier in $Er_3N@C_{80}$ solid at sufficiently high temperatures. In order to clarify the relationship between the energy band structure and the activation energy of the trapped carrier, further experiments such as far infrared (FIR) absorption measurement on the $Er_3N@C_{80}$ material are needed.

V. CONCLUSION

We have studied the carrier transport properties of the nanocrystalline $Er_3N@C_{80}$ sample by measuring temperature-dependent conductivity and current-voltage characteristics. The electrical transport in the nanocrystalline $Er_3N@C_{80}$ sample was governed by space charge limited conduction mechanism which is explained using Poole-Frenkel model. At temperatures above 350 K, the charge carriers during the transport were scatted mainly by acoustic phonon scattering process. On the other hand, ionic scattering was a dominant process in the charge carrier transport at temperatures below 250 K. There were different activation energies of the trapped charge carrier in high and low temperature regions, 16 meV for temperatures above 350 K and 35.5 meV for temperatures below 250 K. The differences on the scattering mechanism and the activation energy of the charge carrier can be explained on the basis of molecular crystal structure and van der Waals interaction between the $Er_3N@C_{80}$ molecules.

ACKNOWLEDGMENTS

This work was partially supported by Project No. 15 – B01, Program of Research for the Promotion of Technological Seeds, Japan Science and Technology Agency (JST). The work was also partially supported by Grant-in-Aid for Exploratory Research No. 23651115, Japan Society for the Promotion of Science (JSPS).

[1]E. Xenogiannopoulou, S. Couris, E. Koudoumas, N. Tagmatarchis, T. Inoue, and H. Shinohara, Chem. Phys. Lett. **394**, 14 (2004).
[2]D. W. Cagle, T. P. Thrash, M. Alford, L. P. F. Chibante, G. J. Ehrhardt, and L. J. Wilson, J. Am. Chem. Soc. **118**, 8043 (1996).
[3]J. Park, A. N. Pasupathy, J. I. Goldsmith, C. Chang, Y. Yaish, J. R. Petta, M. Rinkoski, J. P. Sethna, H. D. Abruna, P. L. McEuen, and D. C. Ralph, Nature **417**, 722 (2002).
[4]T. I. Smirnova, A. I. Smirnov, T. G. Chadwick, and K. L. Walker, Chem. Phys. Lett. **453**, 233 (2008).
[5]W. Harneit, Phys. Rev. A **65**, 032322 (2002).
[6]A. Ardavan, M. Austwick, S. C. Benjamin, G. A. D. Briggs, T. J. S. Dennis, A. Ferguson, D. G. Hasko, M. Kanai, A. N. Khlobystov, B. W. Lovett, G. W. Morley, R. A. Oliver, D. G. Pettifor, K. Porfyrakis, J. H. Reina, J. H. Rice, J. D. Smith, R. A. Taylor, D. A. Williams, C. Adelmann, H. Mariette, and R. J. Hamers, Philos. Trans. R. Soc. London, Ser. A **361**, 1473 (2003).
[7]S. C. Benjamin, A. Ardavan, G. A. D. Briggs, D. A. Britz, D. Gunlycke, J. Jefferson, M. A. G. Jones, D. F. Leigh, B. W. Lovett, A. N. Khlobystov, S. A. Lyon, J. J. L. Morton, K. Porfyrakis, M. R. Sambrook, and A. M. Tyryshkin, J. Phys. Condens. Matter **18**, S867 (2006).
[8]T. A. Murphy, T. Pawlik, A. Weidinger, M. Hohne, R. Alcala, and J. M. Spaeth, Phys. Rev. Lett. **77**, 1075 (1996).
[9]S. Sato, S. Seki, G. Luo, M. Suzuki, J. Lu, S. Nagase, and T. Akasaka, J. Am. Chem. Soc. **134**, 11681 (2012).
[10]O. Tishchenko and D. G. Truhlar, J. Phys. Chem. Lett. **4**, 422 (2013).
[11]S. Y. Yang, M. Yoon, C. Hicke, Z. Y. Zhang, and E. Wang, Phys. Rev. B **78**, 115435 (2008).
[12]S. Stevenson, G. Rice, T. Glass, K. Harich, F. Cromer, M. R. Jordan, J. Craft, E. Hadju, R. Bible, M. M. Olmstead, K. Maitra, A. J. Fisher, A. L. Balch, and H. C. Dorn, Nature **401**, 55 (1999).
[13]H. Shinohara, Rep. Prog. Phys. **63**, 843 (2000).
[14]D. S. Deak, F. Silly, K. Porfyrakis, and M. R. Castell, Nanotechnology **18**, 075301 (2007).
[15]K. Kobayashi, Y. Sano, and S. Nagase, J. Comput. Chem. **22**, 1353 (2001).
[16]M. M. Olmstead, A. D. Bettencourt-Dias, J. C. Duchamp, S. Stevenson, H. C. Dorn, and A. L. Balch, J. Am. Chem. Soc. **122**, 12220 (2000).
[17]C. Nörenberg, D. F. Leigh, D. Cattaneo, K. Porfyrakis, A. Li Bassi, C. S. Casari, M. Passoni, J. H. G. Owen, and G. A. D. Briggs, J. Phys. Conf. Ser. **100**, 052080 (2008).
[18]M. Sakaino, Y. Sun, and F. Morimoto, J. Appl. Phys. **115**, 023701 (2014).
[19]Y. Sun, B. Onwona-Agyeman, and T. Miyasato, Jpn. J. Appl. Phys., Part 1 **50**, 031601 (2011).
[20]N. Karl, Synth. Met. **133–134**, 649 (2003).
[21]D. H. Dunlap, P. E. Parris, and V. M. Kenkre, Phys. Rev. Lett. **77**, 542 (1996).
[22]M. A. Lampert and P. Mark, *Current Injection in Solids* (Academic Press, New York, 1970), p. 27.
[23]J. G. Simmons, Phys. Rev. **155**, 657 (1967).
[24]N. A. Drokin, G. A. Kokourov, G. A. Glushchenko, I. V. Osipova, A. N. Maslennikov, and G. N. Churilov, Phys. Solid State **54**, 844 (2012).
[25]J. R. Macdonaid, Ann. Biomed. Eng. **20**, 289 (1992).
[26]N. A. Drokin, A. V. Fedotova, G. A. Glushchenko, and G. N. Churilov, Phys. Solid State **52**, 657 (2010).
[27]J. K. J. van Duren, V. D. Mihailetchi, P. W. M. Blom, T. van Woudenbergh, J. C. Hummelen, M. T. Rispens, R. A. J. Janssen, and M. M. Wienk, J. Appl. Phys. **94**, 4477 (2003).
[28]C. Tang, W. Zhu, and K. Deng, ACTA Chim. Sinica **67**, 1421 (2009); available at http://sioc-journal.cn/Jwk_hxxb/EN/abstract/abstract329593.shtml.
[29]M. Shiraishi, K. Shibata, R. Maruyama, and M. Ata, Phys. Rev. B **68**, 235414 (2003).
[30]N. Hayashi, H. Ishii, Y. Ouchi, and K. Seki, J. Appl. Phys. **92**, 3784 (2002).
[31]C. Sommerhalter, T. Glatzel, T. W. Matthes, A. Jaeger-Waldau, and M. C. Lux-Steiner, Appl. Surf. Sci. **157**, 263 (2000).
[32]J. M. Campanera, C. B. Marilyn, M. Olmstead, A. L. Balch, and J. M. Poblet, J. Phys. Chem. A **106**, 12356 (2002).
[33]S. Ptasinska, O. Echt, S. Denifl, M. Stano, P. Sulzer, F. Zappa, A. Stamatovic, P. Scheier, and T. D. Mark, J. Phys. Chem. A **110**, 8451 (2006).
[34]A. A. Popov, J. Comput. Theor. Nanosci. **6**, 292 (2009).
[35]G. B. Alers, B. Golding, A. R. Kortan, R. C. Haddon, and F. A. Theil, Science **257**, 511 (1992).
[36]A. F. Hebard, R. C. Haddon, R. M. Fleming, and A. R. Kortan, Appl. Phys. Lett. **59**, 2109 (1991).
[37]C. J. Nuttall, Y. Hayashi, K. Yamazaki, T. Mitani, and Y. Iwasa, Adv. Mater. **14**, 293 (2002).
[38]Y. Iwasa and C. J. Nuttall, Synth. Met. **135–136**, 773 (2003).
[39]B. Pevzner, A. F. Hebard, and M. S. Dresselhaus, Phys. Rev. B **55**, 16439 (1997).
[40]M. Gu, T. Tang, C. Hu, and D. Feng, Phys. Rev. B **58**, 659 (1998).
[41]M. S. Dresselhaus, G. Dresselhaus, and P. C. Eklund, *Science of Fullerenes and Carbon Nanotubes* (Academic, New York, 1996).
[42]R. C. Weast, *CRC Handbook of Chemistry and Physics* (CRC Press, West Palm Beach, FL, 1992).
[43]J. Bardeen and W. Shockley, Phys. Rev. **80**, 72 (1950).
[44]H. Ehrenreich, Phys. Rev. **120**, 1951 (1960).
[45]K. Prassides, H. W. Kroto, R. Taylor, D. R. M. Walton, W. I. F. David, J. Tomkinson, R. C. Haddon, M. J. Rosseinsky, and D. W. Murphy, Carbon **30**, 1277 (1992).
[46]T. Matsuo, H. Suga, W. I. F. David, R. M. Ibberson, P. Bernier, A. Zahab, C. Fabre, A. Rassat, and A. Dworkin, Solid State Commun. **83**, 711 (1992).
[47]L. Pintschovius, B. Renker, F. Gompf, R. Heid, S. L. Chaplot, M. Haluska, and H. Kuzmany, Phys. Rev. Lett. **69**, 2662 (1992).